Serb. Astron. J. № 202 (2021), 1 - 16 **UDC 524.882 : 524.7**
DOI: https://doi.org/10.2298/SAJ2102001K Invited review

INVESTIGATING CLOSE BINARY SUPERMASSIVE BLACK HOLES AT HIGH ANGULAR RESOLUTION

A. Kovačević[1,2]

[1] *Department of Astronomy, Faculty of Mathematics, University of Belgrade Studentski trg 16, 11000 Belgrade, Serbia*

[2] *Fellow of Chinese Academy of Sciences President's International Fellowship Initiative (PIFI) for visiting scientist*

E–mail: *andjelka@math.rs*

(Received: April 28, 2021; Accepted: April 28, 2021)

SUMMARY: Gravitational waves (GW) in the nano-Hz domain are expected to be radiated by close-binaries of supermassive black holes (CB-SMBHs; components bound in a Keplerian binary at mutual distance less than ~ 0.1 pc), which are relicts of galaxy mergers and anticipated to be measured via the Pulsar Timing Array (PTA) technique. The challenge of present CB-SMBH investigations is that their signatures are elusive and not easily disentangled from a single SMBH. PTAs will typically have a glimpse of an early portion of the binary inspiral to catch the frequency evolution of the binary only with sufficiently high mass and initially high eccentricity. Thus, we have to make use of electromagnetic observations to determine orbital parameters of CB-SMBHs and test nano-Hz GW properties. The 2D reverberation mapping (RM) is a powerful tool for probing kinematics and geometry of ionized gas in the SMBHs (single or binary) vicinity, yet it can lose information due to projection on the line of sight of the observer. Nevertheless, spectroastrometry with AMBER, GRAVITY, and successors can provide an independent measurement of the emitting region's size, geometry, and kinematics. These two techniques combined can resolve CB-SMBHs. In this review, we focus on RM and spectroastrometry observational signatures of CB-SMBHs with non-zero eccentricity from recent simulations with particular attention to recent developments and open issues.

Key words. Galaxies: active – Quasars: supermassive black holes – Accretion: accretion disks – Techniques: interferometric

1. INTRODUCTION

Active galactic nuclei (AGNs) are one of the most energetic and powerfull sources in the Universe. The activity is triggered by accretion of material around a super massive black hole (SMBH) in the core of these objects. AGN can be found in galaxies such as ellipticals, disc galaxies, and in a certain fraction of dwarf galaxies (Netzer 2013). Although they are not omnipresent, AGNs are widely accepted as a stage in the life cycle of galaxies (see, e.g. Marconi et al. 2004, Best et al. 2005). Their "extra-power" is unlike the stellar nuclear fusion and is universally assumed to be an actively accreting central SMBH (Zeldovich and Novikov 1964, Salpeter 1964, Rees 1984). Their prominent observational signatures that cover the full electromagnetic spectrum include (see Padovani et al. 2017, for a thorough review): masses $\geq 10^6 M_\odot$; very high luminosities (up to $L_{\rm bol} \sim 10^{48} {\rm erg\,s^{-1}}$), setting them as the strongest non-explosive sources in the observable Universe, detectable up to very high redshifts (currently $z \sim 7.642$, Wang et al. 2021); compact emitting regions ($\sim$ Mpc) in most bands, and broad-band emission covering almost the entire electromagnetic spectrum. In a unified model, an AGN's SMBH is surrounded by a subparsec geometrically thin accretion disc threaded by strong

© 2021 The Author(s). Published by Astronomical Observatory of Belgrade and Faculty of Mathematics, University of Belgrade. This open access article is distributed under CC BY-NC-ND 4.0 International licence.

magnetic fields and a dusty torus (Antonucci 1993, Urry and Padovani 1995). The clouds with Keplerian motion populate two distinctive regions: the broad-line region (BLR) and the narrow-line (NLR) region. Many observational studies indicate the range of $10^3 - 10^4\,\mathrm{km\,s^{-1}}$ as Keplerian velocity of the BLR clouds (see e.g., Blandford et al. 1990, Peterson 1998). Emission lines of atomic gas in BLR clouds are a hallmark of active SMBH since they trace the gravitational potential of the SMBH. Substantial monitoring campaigns use light echoes (BLR emission light curves), a technique called reverberation mapping (RM, Blandford and McKee 1982), to measure the BLR size and infer other physical properties, with ongoing work expanding the AGN sample size from tens (see, e.g., Peterson et al. 2004, Ilić et al. 2017, for a thorough review of Serbian AGN group contribution) to hundreds (Grier et al. 2017, Du et al. 2018b). The top result of the RM studies is that the size of the BLR scales with the square of luminosity, $R_{\mathrm{BLR}} \sim \sqrt{L}$ (see the review in Popović 2020). However, RM provides this and other important AGN scaling relations locally (redshift $z < 0.3$) and probed a narrow SMBH mass range, typically $10^{7-8} M_\odot$ (Bentz 2016). These local relations are then extrapolated to a much higher redshift and for larger SMBH masses ($10^{9-10} M_\odot$). However, for monitoring non-local AGN, RM should cover an observational time baseline of decades to recover the reliable BLR dimensions since the dynamical time scales and cosmological time dilation $\sim (1+z)$ increase the observed dimensions (Kaspi et al. 2007). This obscures knowledge of the galaxy/SMBH co-evolution and of the high redshift SMBHs population in general. Additionally, assumptions about the geometry of BLR components may bias the inferred physical interpretation (Mangham et al. 2019). Thus, an independent method to detect the BLR structure is needed. In this light, interferometry is a newly-introduced independent method for spatially resolving AGN (Swain et al. 2003, Jaffe et al. 2004, Wittkowski et al. 2004). The main components of AGN, as projected on the sky, are of small angular dimension, from micro (μ) to milli (m)- arcsecond (as) scales, requiring long baselines. Being extragalactic objects at large distances, AGNs are also relatively faint sources for observations, thus only observed in optical interferometry with 8–10-metre-class telescopes and instrumentation with premium sensitivity (Hönig et al. 2018). Continuum measurements provide information about hot dust surrounding the nucleus (Kishimoto et al. 2011, Weigelt et al. 2012). The second-generation Very Large Telescope Interferometer (VLTI) instrument GRAVITY has enormously enhanced sensitivity and coverage by combining information from four telescopes in a six-baseline array configuration (GRAVITY Collaboration 2020a). GRAVITY Collaboration (2020b) used data from GRAVITY ongoing the AGN observing program to measure hot dust region sizes for eight of the brightest type 1 AGN, almost doubling the sample for which the near-infrared (NIR) interferometry is available. However, the BLR is much smaller (angular size < 0.1 mas) than the hot dust region and is unresolvable even with the VLTI. Instead, its kinematics is imprinted as the photocentre shift of atomic gas in the BLR relative to the hot dust ring across the emission line's wavelength (or radial velocity). The photocentre shift can be measured via a small differential phase signal $< 1°$ (Rakshit et al. 2015) whose detection requires deep integrations. Spatially resolving the tiny size of the BLR, $10^3 - 10^5$ gravitational radii (Netzer 2015), has been the long-term task of spectroastrometry (Petrov et al. 2001, Marconi et al. 2003), which is now possible with GRAVITY.

GRAVITY Collaboration (2018) made the first robust measurements of the BLR size and kinematics for 3C 273 by combining differential phase with the Paα emission line profile. These measurements are complementary with the BLR model as a thick rotating disc in the gravitational well of SMBH $\sim 3 \times 10^8 M_\odot$ which is further entirely consistent with the result of decade-long RM. IRAS 09149−6206 is the second source, following 3C 273, for which the NIR interferometric observations provided the size of the BLR and an estimate of the mass of the central black hole (GRAVITY Collaboration 2020c). The BLR size of $\sim 65\,\mu$as is consistent with the radius–luminosity relation based on Hβ RM of AGNs. With all of this in mind, the GRAVITY instrument has proven that the NIR interferometry is a robust device to probe the innermost regions of AGN on subparsec scales. At such scales, the NIR interferometry is capable of opening the window for exploration of the close-binary SMBH (CB-SMBH). By providing information from spatial dimension, the upgraded GRAVITY+ instrument will ultimately resolve the binarity of AGNs (GRAVITY+ Collaboration 2019) that are expected in thousands from surveys such as SDSS-V (Kollmeier et al. 2019) and 4MOST (Swann et al. 2019). Generally, the GRAVITY observations through spectroastrometry sensitively detect the angular structure of the BLR in a direction perpendicular to line-of-sight (LOS), whereas the RM observations are more sensitive along the direction of sight. Combined observables of these two techniques can give information on the distance and 3D structure of the emitting region. The dual AGNs appear among galaxies frequently (Wang et al. 2019) based on examination of the double-peaked features of the [O III] line found in SDSS quasars (Wang et al. 2009). However, CB-SMBHs signatures are ambiguous (Popović 2012, De Rosa et al. 2019, Wang and Li 2020). Nevertheless, we are aware that most of AGN features can be explained by individual SMBHs accretion (Rees 1984), indicating that most CB-SMBHs have probably finished their final coalescences (Wang and Li 2020). Several observational signatures have been used to search for CB-SMBH candidates (De Rosa et al. 2019). For example, there are notable attempts to resolve the periodic signal in light curves with a very long time baseline covering several decades (see Bon et al. 2012, Li et al. 2016, Bon et al. 2016, Li et al. 2019). A few hundreds of CB-SMBH candidates have been identified from systematic searches

over extensive time-domain surveys (Graham et al. 2015, Charisi et al. 2016, Liu et al. 2016) and time series analysis of decadal AGN long term monitorings (see e.g., Kovačević et al. 2017, 2018, 2019, 2020c,d). From theory of the hierarchical mergers of galaxies, CB-SMBHs emerging from dual galactic cores must be formed at centers of some (if not all) galaxies for certain periods of evolution (Begelman et al. 1980, Wang and Ip 2020). Also, some other types of AGN such as Changing-look AGN (CL-AGNs) as a new subpopulation (see e.g. notable case of NGC 3516, Shapovalova et al. 2019, Ilić et al. 2020, Feng et al. 2021) challenge some fundamental physics of AGNs so that a possible explanantion for them is that CB-SMBHs with high eccentricities are able to trigger the CL transition through one orbit (see Wang and Bon 2020). This review focuses on RM and spectroastrometry observational signatures of CB-SMBHs with non-zero eccentricity from numerical simulations with particular attention to recent developments and open issues. The outline of this work is as follows. In Section 2, we described the general formalism of Keplerian bound SMBHs binaries. In Section 3, we described modeled kinematics and reverberation maps of CB-SMBH. In Section 4, we introduce optical interferometry, emphasizing the modeled observables of differential interferometry of CB-SMBH. The feasibility of present and future RM and optical interferometric observation of the CB-SMBHs with current and future instruments is discussed in Section 5. The work is summarized in the last section.

2. GENERAL FORMALISM

Here we introduce the generic evolutionary pathway of CB-SMBHs, and geometric configurations of CB-SMBH systems. We adopt the following notation: a bold font variable refers to a 3×1 vector, and unless otherwise specified, the indices $k = 1, 2$ are used to discern the primary and secondary components' parameters. The cloud parameters are identified with the subcript c, which can be followed by numerical index $k = 1, 2$ if a cloud is in the BLR of primary or secondary. If all clouds in the disc-like BLR share the same quantity of a particular parameter, it will be indicated by subscript c. We assume M_1 and M_2 to be the primary and secondary SMBH masses ($M_1 > M_2$), respectively with CB-SMBH mass ratio:

$$q = \frac{M_2}{M_1} < 1.$$

In our RM and interfeormetric models, the input parameters are five orbital elements defining the size and shape $(a, e, i, \Omega, \omega)$ of orbit and time t, while the output parameters are position $(\boldsymbol{r}(t))$ and velocity $(\dot{\boldsymbol{r}}(t))$ of objects (both SMBH and each cloud in the BLRs) obtained by solving Kepler's equation (all parameters definitions are given in Kovačević et al. (2020a,b):

$$\{a, e, i, \Omega, \omega, \mathcal{M}, t\}_k \Rightarrow \mathrm{Kepler's\,Eqn.} \Rightarrow \quad (1)$$

$$\{\boldsymbol{r}(t), \dot{\boldsymbol{r}}(t)\}_q, k = 1, 2, \quad (2)$$

where $\mathcal{M}$ is the mean anomaly. The barycentric vector $\boldsymbol{n}$ defines the line of sight. Then the binary inclination angle to the observer is $\cos i_0 = \boldsymbol{n} \cdot \boldsymbol{J}_{\rm bin}$ where $\boldsymbol{J}_{\rm bin}$ is the normalized orbital angular momentum vector of the CB-SMBH system.

2.1. Evolutionary pathway

Substantially observations of galaxies and AGNs in the electromagnetic Universe focus on the cosmic high noon, a period around $z \sim 1.5 - 3$. This epoch features several critical transitions in galaxy evolution, of which galaxy mergers drive the formation of supermassive binary black holes (Begelman et al. 1980, Volonteri et al. 2003). In the merger remnant, the evolution of SMBHs develops in three phases, each characterized by a distinct physical process. Dynamical friction (Chandrasekhar 1943, Just et al. 2011) triggers sinking of SMBHs in the merger remnant, making SMBHs close enough that they form a binary system (Fig. 1 top pane). This occurs on the Chandrasekhar dynamical friction time-scale:

$$t_{\rm df}\,[{\rm yr}] \sim \frac{4\times10^6}{\log N}\frac{\sigma_c}{200\,{\rm km\,s^{-1}}}\left(\frac{r_c}{\rm pc}\right)^2 M_8^{-1} \quad (3)$$

where $M_8 = \frac{M_1}{10^8 M_\odot}$is the primary mass, the galaxy core is presumed to have a velocity dispersion σ_c, a radius r_c and confines N stars. The binary orbital energy is extracted efficiently by this process until the binary reaches the hard stage. This stage assumes a binary orbital separation

$$a < \frac{G\mu}{4\sigma_c^2},$$

where G is the gravitational constant and

$$\mu = \frac{M_1 M_2}{M_1 + M_2}$$

is the reduced mass of the system. At this point in evolution, the dynamical friction diminishes, while SMBHs are at mutual parsec scale distances.

In the second phase, stars on orbits intersecting the binary orbit drain out binary's orbital energy by the slingshot during three-body encounters shrinking the binary orbit. If it is efficient to bring the SMBHs in the binary close enough (milliparsec - subparsec separations), the pair becomes CB-SMBH (Fig. 1 middle pane). At this stage, both SMBHs will decouple from external influences and perhaps evolve primarily via the emission of GWs as a pure two-body system. Due to this decoupling, the GWs frequencies lie in the nano-Hz band, well below any ground-based, the but pulsar-timing arrays (PTAs) can directly probe these frequencies. In the third and final phase, GW emission takes out the remaining orbital energy in the binary leading the SMBHs to coalesce (Fig. 1 bottom pane).

Identification of the CB-SMBHs provides us with essential constraints on the interaction processes that govern the shrinkage of the binary beyond the final

parsec. CB-SMBHs are so close (∼0.01 pc) that they are difficult to image using current optical technology. Various signatures have been used to search for and identify binary candidates (Fig. 2).

As shown by Wang et al. (2020), except for interferometry, another promising technique is a joint analysis of the interferometry and RM observations. The circumbinary discs may also offer electromagnetic signatures. In particular, these two signatures have not been explored and applied on AGNs in depth so far. Thus, they can be most likely to drive observational efforts shortly in this field.

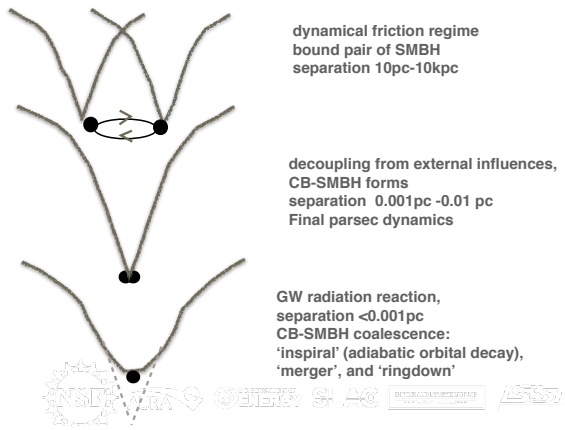

Fig. 1: Scheme of three crucial stages of the binary SMBHs evolution following a galaxy merger. Here we focus on electromagnetic signatures of the second stage when CB-SMBH forms (middle pane).

2.2. Geometry

The two fundamental components constitute the CB-SMBH systems: (1) circumbinary disc (CBD) and (2) emission-line regions. Unlike a single SMBH, the two components are confined by the joint potential of the CB-SMBHs system. We assume a standard geometrically thin, optically thick, steady-state accretion disc model for the CBD, coplanar with the binary orbit. A residence time $t_{\rm res} \sim |d\ln a/dt|^{-1}$ is determined by orbital decay and it is associated to each phase of the forming binary SMBH. This is the fraction of time that a binary with specific characteristics (mass, mass ratio, orbital period) spends at a given orbital separation during its lifetime. Since the bright phase of AGN (order of several 10^7 yrs, Martini 2004) is of the order of time scale of the binary evolution from the outer edge of the CBD to coalescence (Haiman et al. 2009), the binaries with separations in this entire range are distributed so that a larger fraction of sources will populate longer $t_{\rm res}$, and a smaller fraction will be found at shorter $t_{\rm res}$ (Charisi et al. 2016). Based on Haiman et al. (2009), for a fixed orbital period, $t_{\rm res}$ relates only to the mass of the binary $M_1 + M_2$ and the (unknown) mass ratio $q = M_2/M_1$ of the binary.

Fig. 3 illustrates the residence time for different orbital periods and redshifts. The lines show the evolution of binary residence time, with total mass $M_1 + M_2 \sim 10^8 M_\odot$, as the orbital motion decays from longer to shorter orbital periods, for three different mass ratios (red line for $q = 1$, black for $q = 0.5$ and green for $q = 0.05$). The segments with different gradients roughly correspond to distinct stages of the binary evolution. At long orbital periods, the binary evolution is slow and dominated by angular momentum exchange with the CBD, whereas at short orbital periods, the binary enters the GW-driven regime and the evolution is faster. The shaded region distinguishes the parts of the binary evolution accessible for study, assuming homogenous cadence and 10 yr monitoring campaign. The classical setup of the BLR is a virialized distribution of clouds, with evidence that many are rotating systems. A variety of RM observations suggest that the fast-rotating BLRs are flattened while slower rotating BLRs are more spherically distributed due to turbulence (see GRAVITY Collaboration 2020c, and references therein). Additionally, the GRAVITY observations of 3C 273 currently support the simplest model. The BLR size of each SMBH in the binary is described by $R_{\rm BLR} \sim L^{0.5}$ relation conditioned by the photoionization process, also depending on accretion of the components, which is given by

$$R_{\rm BLR} \sim 3.8\kappa^{-0.5}\lambda_{\rm E}^{0.5} M_6^{0.5} \quad (4)$$

where $M_6 = M_{SMBH}/10^6 M_\odot$, the bolometric correction is κ, the Eddington ratio is $\lambda_{\rm E} = \frac{\eta \dot{M} c^2}{L_{\rm E}}$ with the radiative efficiency η , the mass accretion rate $\dot{M}$, and Eddington luminosity is $L_{\rm E} = 1.44 \times 10^{44} {\rm erg\,s{-}1}$. For circular binaries $e_i = 0$ and semi-major axes a_i, the relative distance of two components is time independent:

$$|r(e_1 = 0, e_2 = 0)| = a, \quad (5)$$

where $a = a_1 + a_2$.

In the circular case, the velocities of SMBHs and their relative velocity are also time-independent. However, in elliptical configurations of clouds in the BLR of CB-SMBH on elliptical orbits, the positions and velocities depend on time and osculating orbital elements. Our model accounts for all these parameters, as explained in Kovačević et al. (2020a,b).

3. REVERBERATION MAPPING OF CB-SMBH

Reverberation mapping (RM) is a well-tested tool for measuring the kinematics of ionized gas around SMBHs. RM is based on the following assumptions (see, e.g., Peterson 2014): (1) the ionizing photons originate from a point source much smaller than the BLR; (2) photoionization is the dominant mechanism producing the emission lines; and (3) the BLR is relatively stable on the RM timescales. Even if broad-line profiles in the CB-SMBH and single SMBH cases could be similar, investigations of Popović et al. (2000), Shen and Loeb (2010) generally show that

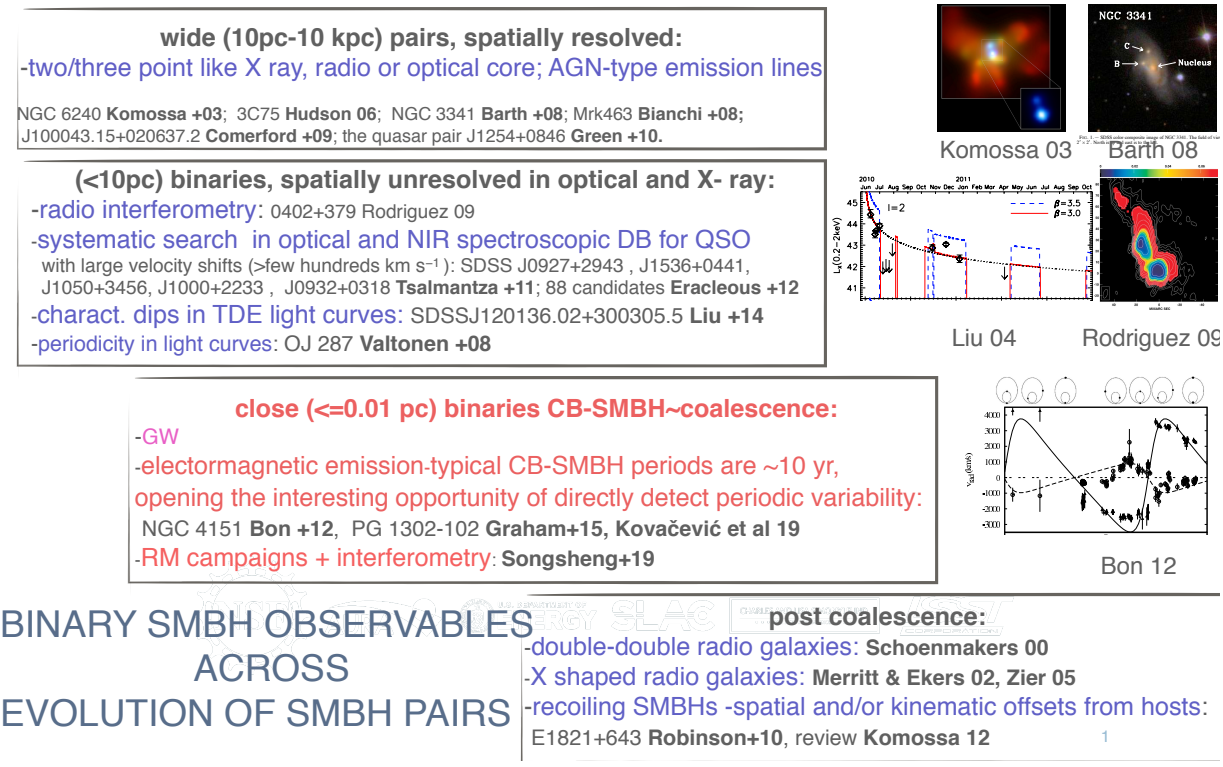

Fig. 2: Diagram of explored signatures of binary SMBH up to now. Electromagnetic emission of circumbinary disc and synergy between reverberation mapping and interferometry are most likely drivers for nearby future CB-SMBH observations.

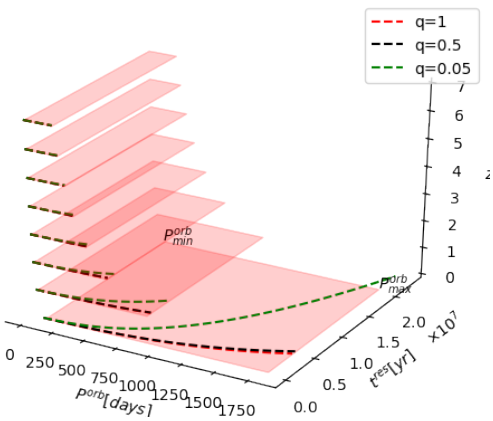

Fig. 3: Residence time of a binary SMBH with total mass of $\sim 10^8 M_\odot$, for mass ratios $q = 1$, $q = 0.5$, $q = 0.05$ denoted with red, black, and green color, respectively. The red regions emphasize the observable orbital period.

they reverberate differently to the continuum variations. Wang et al. (2018) provided the first semi-analytical formulae for two-dimensional (2D) transfer functions (TFs) of emission lines to continuum in circular CB-SMBH models, in contrast with single SMBH cases.

However, Kovačević et al. (2020a) extended this formalism to account for CB-SMBH with non-zero eccentricity. In the simple linear theory, the broad emission-line radial velocity V_z, and time dependent response $\mathcal{L}(V_z, t)$ is a convolution of prior, time delayed continuum variations $\mathcal{C}(t-\tau)$ with a transfer function $\Psi(V_z, \tau)$ such that (Blandford and McKee 1982):

$$\mathcal{L}(V_z, \tau) = \int_{-\infty}^{+\infty} \mathcal{C}(t-\tau)\Psi(V_z, \tau)d\tau. \qquad (6)$$

The TF is a projection of a six-dimensional (three spatial and three kinematical) phase space distribution into 2D phase space (defined by radial velocity V_z and time lag τ). The contribution of a particular cloud of single BLR to overall response depends on: its distance from the continuum source (setting the time delay of its response); its radial velocity (i.e. the velocity at which its response is observed); and emissivity (a parameter describing cloud efficiency of the reprocessing continuum into line photons in a steady-state).

Thus, the TF for a single elliptical disc can be written as follows:

$$\Psi(v, \tau) = \int \epsilon(\varrho)\delta(v - \mathbf{V}\mathbf{n}_{\rm obs})\delta(ct - (|\boldsymbol{\varrho}| - \boldsymbol{\varrho}\cdot\mathbf{n}_{\rm obs}))\mathrm{d}\boldsymbol{\varrho}\,\mathrm{d}\mathbf{V}, \qquad (7)$$

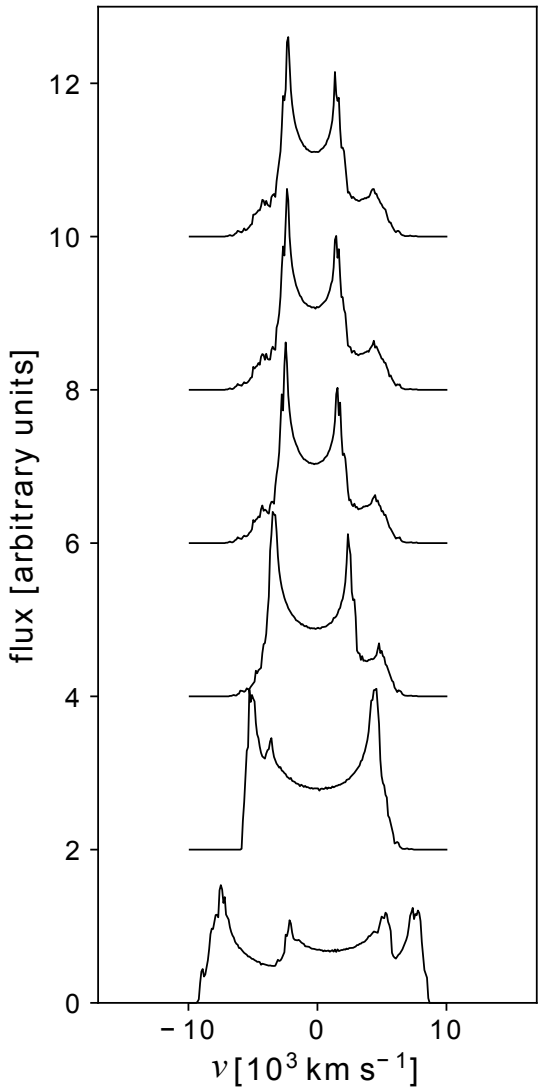

Fig. 4: Series of line profiles corresponding to theoretical 2D transfer function map obtained for coplanar elliptical CB-SMBH with $M_1 = 10^8 M_\odot, M_2 = 0.5 \cdot 10^8 M_\odot, e = 0.5, \Omega_1 = \Omega_2 = 0°, \omega_1 = 0°, \omega_2 = 180°$. Orbital parameters of the clouds in both BLRs are $\Omega_c = 100°, \omega_c = 0°, 180°$ and eccentricities are random. From bottom to top spectra are sampled in time instances $t_i = \frac{kP}{12}, k = 0, ..., 6$ where P is the orbital period.

where $\epsilon\varrho$ is the responding volume emissivity (assumed isotropic) of the emission region as a function of position, and $\boldsymbol{\varrho}, \mathbf{V}$ are barycentric state vectors of a cloud. We adopted the emissivity law $\epsilon(\varrho) = \epsilon_0 \varrho^{-q}$ (see Eracleous et al. 1995, and references therein), where ϱ is a polar form of trajectory of the cloud determined for given time span from solution of Kepler's equation. Since the orbital plane of a cloud is defined by inclination (i) and longitude of the ascending node (Ω) of its orbit, the TF of the elliptical disc can be given as follows:

$$\Psi(v,\tau) = \epsilon_0 \int_{R_i}^{R_o} \varrho^{-q} d\varrho \int_0^{2\pi} d\Omega \int_{-i_{\min}}^{i_{\max}} \sin i \, \mathrm{d}i \int_0^{2\pi} \delta(X_1)\delta(X_2)\mathrm{d}E \quad (8)$$

where $X_1 = v - V_z, X_2 = ct - c\tau$, and E is the eccentric anomaly of a cloud in its orbital plane. Limits of integration $i_{\min}, i_{\max}$ indicate the range of the clouds orbit inclination in a disc-like BLR, so that $\Theta = |i_{\max} - i_{\min}|$. Then, the composite TF for CB-SMBH with non-zero eccentricity is obtained by deriving $\Psi_1(v,\tau)$ and $\Psi_2(v,\tau)$ for each BLR and coupling them as follows:

$$\Psi(v,\tau)_{\text{coupled}} = \frac{\Psi_1(v,\tau)}{1+\Gamma_0} + \frac{\Psi_2(v,\tau)}{1+\Gamma_0^{-1}}, \quad (9)$$

where Γ_0 is the coupling factor obtained by normalization of the continuum variation of one of SMBH with continuum of another SMBH. Here we used the constant $\Gamma_0 \sim 1$ as the simplest case when the binary black holes have the same properties of continuum variations. The masses of components are $M_1 = 10^8 M\odot, M_2 = 0.5 \times 10^8 M\odot$. We let the pericenters of clouds orbit be uniformly distributed for BLR around a primary $(R_\mathrm{i}, R_\mathrm{o}) = (7, 15)$ lightdays (ld) and a secondary component $(R_\mathrm{i}, R_\mathrm{o}) = (4, 10)$ ld. The inclination range for cloud trajectories in both BLR is $\sim 5-7$ degrees. This assumption agrees with the hypothesis that near coplanar accretion discs and BLR could be expected in gas-rich mergers (Bogdanović et al. 2007). An illustration the velocity-resolved 2DTF produced by the biconical configuration in BLRs of both SMBHs is shown in Fig. 5. In this configuration, the emitting clouds are confined to two opposing cones, aligned on a common axis passing through the continuum source in each BLR. The axis can be inclined at different angles to the line of sight, and both cones have the same opening half-angle. The approaching and receding flows produce a distinctive bifurcated structure with paired blades for each SMBH in the system. Smaller horizontal and upward blades correspond to the biconical configuration of clouds in SMBH with a smaller mass. The blades are wide, and their angular separation is greater since the cone angle is larger (30°). In contrast, at a larger inclination, $i = 90°$, both blades are almost vertical and overlapped, making discernment of the SMBH components difficult.

Fig. 6 shows a 2DTF map for coplanar elliptical binary SMBH orbits with disc-like BLRs at two different positions during their mutual motion (Kovačević et al. 2020a). The maps are deformed bell shapes, which are distinctive from biconical blades.

Kinematics derived from our elliptical BLR models and binary geometry are reduced to circular signatures when eccentricity and orbital orientation parameters are set to zero. Fig. 4 shows an example of a series of velocity profiles obtained by integrating 2DTF when orbital eccentricities of clouds in both BLRs are random. One of the prominent spectral features of the eccentric CB-SMBH observed by

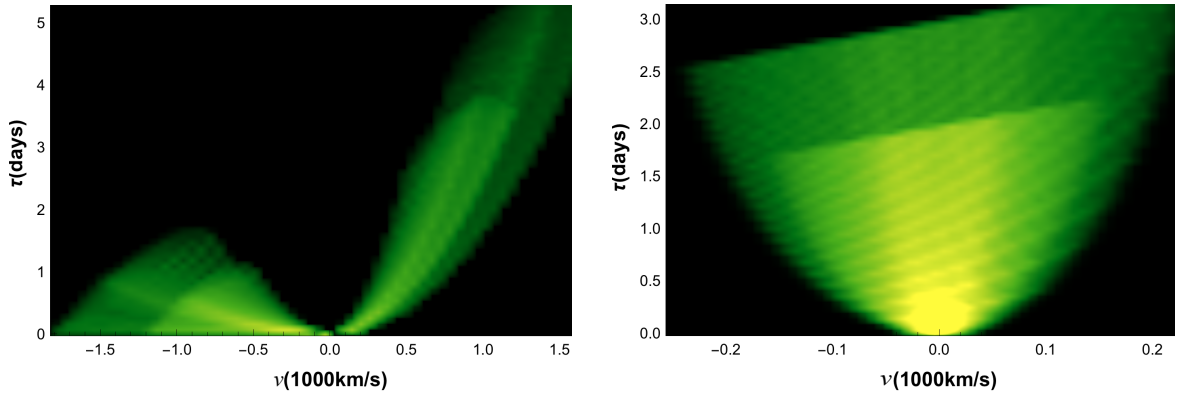

Fig. 5: 2D Transfer function of CB-SMBH with clouds in biconical geometry. Parameters of model: $M_1 = 10^8 M_\odot, M_2 = 0.5 \times 10^8 M_\odot, e = 0.9$, the conical opening angle is 30°, (7,15) ld and (4,10) ld are the inner and outer boundaries of the primary and secondary BLR, respectively. Clouds are on circular orbits around the axis of cone with inclinations $(-7°, 7°)$ *Left*: The cone axis inclined by 45°. *Right*: The cone axis inclined by 90°. Radial velocity and time lags of clouds in BRLs are given in x and y-axis, respectively.

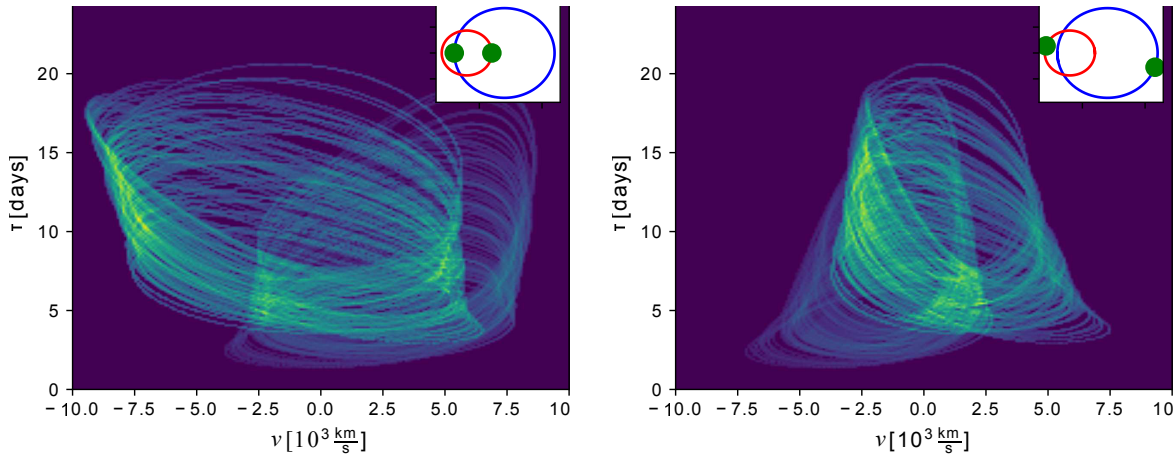

Fig. 6: 2DTF maps obtained for coplanar CB-SMBH with disc-like BLRs. Inset plots present orbital phase of the binary system corresponding to the map. Direction of motion of the binary SMBH is anticlockwise Model parameters are: a coplanar elliptical binary system with $e = 0.5$, $\Omega_1 = \Omega_2 = 0°$, $\omega_1 = 0, \omega_2 = 180°$, clouds orbits in both BLRs have random eccentricities and $\Omega_{c1} = \Omega_{c2} = 100°, \omega_{c1} = 110°, \omega_{c2} = 290°$. Figure adopted from Kovačević et al. (2020a).

Kovačević et al. (2020a) is an intermediate peak when clouds orbital eccentricities are randomized. This intermediate peak can be more or less visible depending on the orbital phase and on the random realization of eccentricities (compare Fig. 4 vs. Fig. 5 in Kovačević et al. (2020a)). This spectral line feature has been observed in spectral lines of a few objects: 3C 390.3 by Popović et al. (2011, see their Fig. 1), Arp 102B by Popović et al. (2014, see their Fig. 3), NGC 4151 by Shapovalova et al. (2008, see their Fig. 6) and E1821+643 by Shapovalova et al. (2016, see their Fig. 15). Interestingly, NGC 4151 and E1821+643 have been seen as binary SMBH candidates (e.g. see Gaussian process analysis in Kovačević et al. 2017, 2018, and references therein). In contrast, spectral lines of a circular CB-SMBH with the eccentric cloud orbit in Fig. 7 show a gradual change of spectral lines over the orbital motion, with less prominent auxiliary features (i.e., an intermediate peak).

Kovačević et al. (2020a) show that rising the inclination of the elliptical orbit of more massive SMBH and decreasing the angle of pericenter of clouds orbits which have random eccentricities blurs the contribution of emission of smaller SMBH. However, in the same non-coplanar settings of the binary system, if we randomize orientations of clouds in both BLRs and eccentricities of clouds of more massive SMBH are more significant than those of smaller SMBH, the contribution of less massive SMBH to the spectral line is less apparent with the hint of its presence seen as asymmetry of line profiles. On the other hand, ran-

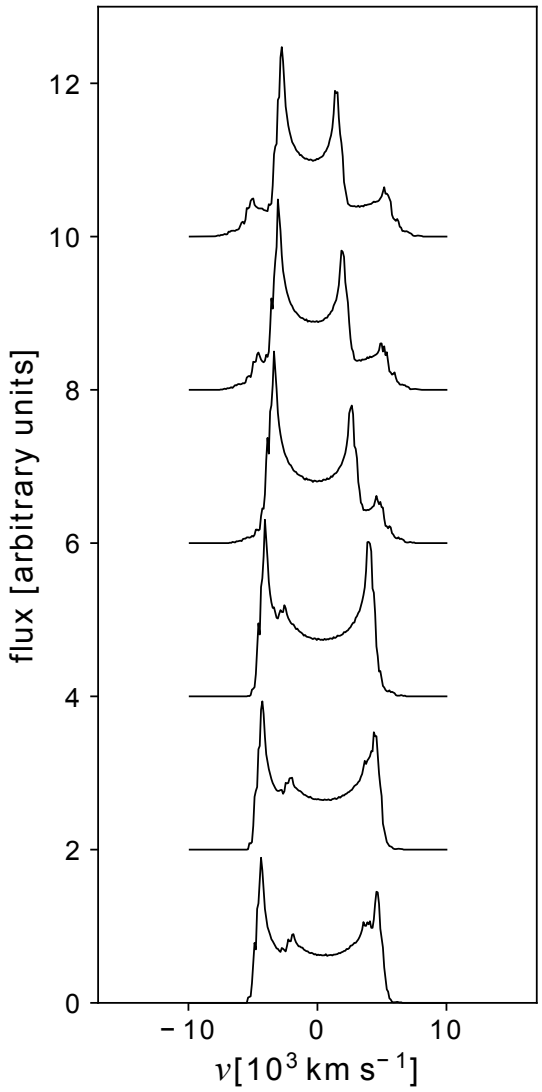

Fig. 7: The same as Fig. 4 but for circular CB-SMBH.

domization of eccentricities and orientations of clouds in both BLRs of non-coplanar CB-SMBH can diminish the contribution of smaller SMBH at the middle and at the end of the orbital period. It is hard to justify the presence of kinematic features of CB-SMBHs through the spectra and 2DTF map alone. This goal depends on several RM campaign factors: (1) homogeneous and high cadence, (2) reasonable spectral resolution, and (3) spectral calibration should be improved for the shape changes of the Hβ profiles ([O III] is then a poor calibrator for this goal). Given the observed TFs from RM campaigns, we can directly compare them with the atlases to select the candidate CB-SMBHs and roughly infer the geometry and kinematics of the constituent BLRs.

4. INTERFEROMETRY OF CB-SMBH

Uncertainities of interferometric differential phase measurements are reduced in the case of narrow spectral lines and they are not contaminated by the wavelength-independent errors (see Waisberg et al. 2017). We modelled the differential phases from the computed brightness distribution of BLRs based on the Zernike-van Cittert's theorem (Petrov 2012):

$$F(\mathbf{u}) = \iint I(\sigma) e^{-2\pi i \sigma, \lambda \mathbf{u}} d\sigma, \tag{10}$$

where F is the flux of object, I is the object intensity distribution, $\boldsymbol{\sigma} = (\alpha, \delta)$ are the object coordinates in the sky and $\mathbf{u} = \mathbf{B}/\lambda = (u, v)$ is the baseline vector of the interferometer. Let the moments of $I(\boldsymbol{\sigma})$ are given as:

$$\mu_{\mathbf{p}} = \int I(\boldsymbol{\sigma}, \lambda) \sigma^{\mathbf{p}} d\boldsymbol{\sigma}, \tag{11}$$

where $\mathbf{p} = (p, q)$, $\boldsymbol{\sigma}^{\mathbf{p}} = \alpha^p \delta^q$. We can expand the complex term in Eq. 10 via Taylor series if $|\boldsymbol{\sigma}\mathbf{u}| << 1$:

$$e^{-2\pi i \boldsymbol{\sigma}\mathbf{u}} = \sum_{l=0}^{\infty} \frac{(-2\pi)^l (\boldsymbol{\sigma}\mathbf{u})^l}{l!}. \tag{12}$$

Taking into account the above complex term we can write definition of the complex visibility $V(\mathbf{u}) = \frac{F(\mathbf{u})}{F(0)}$ as:

$$V(\mathbf{u}) \sim 1 - 2\pi i \mathbf{u} \Xi, \tag{13}$$

where

$$\Xi = \frac{\int I(\boldsymbol{\sigma}, \lambda) \boldsymbol{\sigma} d\boldsymbol{\sigma}}{\int I(\boldsymbol{\sigma}) d\boldsymbol{\sigma}}. \tag{14}$$

Then, the phase of visibility is $\arg(V(\mathbf{u})) \sim -2\pi \mathbf{u} \Xi$. However, the phase can be disrupted by the atmospheric turbulence when only one baseline (two telescopes) is used. This problem can be reduced with the differential phase $\Delta\phi$ (see e.g. Delaa et al. 2013, and references therein). The differential phase is defined as the difference between the fringe phases obtained in two spectral channels centred on wavelengths λ and λ_r (a wavelength of a reference channel), respectively:

$$\Delta\phi = -2\pi \boldsymbol{u} \cdot (\boldsymbol{\Xi}(\lambda) - \boldsymbol{\Xi}(\lambda_r)). \tag{15}$$

This quantity is particularly relevant for line profiles when accounting the kinematics of the source, and the continuum region is the natural choice as a reference so that $\xi(\lambda_r) = 0$ (see Kovačević et al. 2020b, and references therein).

It has been shown both empirically (see e.g., GRAVITY Collaboration 2018, 2020a,b,c) and theoretically (Songsheng et al. 2019) that differential interferometry can follow a variation of the BLR photocentre. It is an underexploited astrophysical parameter in the AGN investigation, with an interpretation similar to the BLR spectral lines. Given the geometry and kinematics of a BLR, its $I(\sigma, \lambda)$ can be calculated

for one broad emission line with the observed central wavelength λ_c as:

$$I(\sigma,\lambda')_l = \int \frac{\epsilon F_c}{4\pi r^2}\mathcal{D}(\mathbf{r},\mathbf{V})\delta(\sigma-\sigma')\delta(\lambda-\lambda')d\mathbf{r}d\mathbf{V},$$

where ϵ is a reprocessing coefficient at cloud position $\mathbf{r}$, F_c is the ionizing flux received by the observer, $\mathcal{D}(\mathbf{r},\mathbf{V})$ is the velocity distribution, $\sigma' = (\mathbf{r}-(\mathbf{r}\cdot\mathbf{n})\mathbf{n})/D$, n is a unit vector defining the line of sight of the observer, $\lambda' = \lambda_c\gamma(1+\mathbf{V}\mathbf{n}/c)(1-\frac{R_S}{r})^{-0.5}$, γ is the Lorentz factor, R_S is the Schwarzschild radius and D is the distance to the object. We have included the relativistic and transverse Doppler shift and the gravitational redshift, since these effects could impact the emission line shape (see GRAVITY Collaboration 2018, and references therein). The global intensity is obtained by adding the emission line and continuum intensities $I_{tot} = I_{\rm cont} + fI_l$.

For a Keplerian BLR with the clouds orbital eccentricities $e = 0.5$ model, the intensity distribution for the Paα line spectral channel is given in Fig. 8. All clouds orbits have the same focus where SMBH is located. The cloud velocity field distributions are chosen to decrease radially from the focus, and the significant emission occurs in the vicinity of the pericenter.

Fig. 9 shows the spectrum, the interferometric differential phase and differential visibility for a single SMBH BLR model given in Fig. 8 and considering an interferometric basline $U(B = 100\text{m}, PA = 90°)$. We take a typical GRAVITY baseline as $B = 100$m and we assume that the baseline is perpendicular to the binary rotation axis ($PA = 90°$) so that the baseline B is along the photoncenter displacement for a pure Keplerian binary (Rakshit et al. 2015, Songsheng et al. 2019).

The difference between the line and the continuum photocentre grows as the line rises, vanishes in the line center, and reverses in the second half of the line. This gives a typical S-shape differential phase where the peaks are more prominent due to the clouds' elliptical motion than in a circular case. The differential visibility globally displays a w-shape modified due to the elliptical motion of clouds. Songsheng et al. (2019) showed that interferometric observables could be modeled for the circular CB-SMBH case. The interferometric model of the CB-SMBH system is a composition of two sources (their BLRs) considered either as point-like or disc-like models with assumed morphologies. Kovačević et al. (2020b) estimated signatures of the elliptical orbital motion of clouds in the BLR of a single SMBH and elliptical orbital setup of CB-SMBH on spectro-interferometric observables. In addition, they investigated the evolution of these observables with different combinations of orbital and geometrical parameters. The general expression for the complex visibility of a binary system is given by:

$$V(\mathbf{u}) = \frac{\sum_{j=1,2} F_j V_j(\mathbf{u}) e^{2\pi\mathbf{u}\boldsymbol{\sigma}}}{\sum_{j=1,2} F_j} \tag{16}$$

where $V_j(\mathbf{u})$ and F_j are the normalized visibility and flux for each individual component, respectively. Fig. 10 shows the interferometric observables for CB-SMBH with both unresolved components.

In this model, the larger SMBH is inclined by 5 degrees to the smaller SMBH orbital plane. This leads to degeneracy in spectral line (Fig. 10) so it is almost indistinguishable from a single SMBH (Fig. 9). However, some slight distinctions are recognizable. Namely, the deep between the horns are caused by velocity fields of clouds but with more prominence in CN-SMBH due to the superposition of projection of velocity fields of clouds in both SMBHs. However, the binary differential phase is distinctive due to the CB-SMBH configuration. Also, the squared visibility indicates the binarity of the system.

Kovačević et al. (2020b) constructed exhaustive atlases of the differential 'zoo' phases for single SMBH and CB-SMBH systems. For a single SMBH, the differential phases resemble a deformed S shape, indicating the rotational and an elongated motion of clouds in BLR. Larger values of Ω and ω induce an increase in amplitude of the differential phase. The peaks are deformed due to the superposition of trigonometric functions of angles controlling the orbital shape. In addition, an increasing cloud orbital inclination produces differential phases with smaller amplitudes. These distortions are an illustrative proof of presence of asymmetry in the disc.

Assuming non-randomised motion, we show in Fig. 11 spectral lines and differential phases for the CB-SMBH model. The clouds' orbital inclinations have uniform distribution $i_c = \mathcal{U}(-5°, 5°)$. Model parameters are for the left plot $\Omega_c \in \mathcal{U}(10°, 90°), \omega_c = 110°, i_c \in \mathcal{U}(-5°, 5°), e_c = 0.5, i_0 = 45°$. Model parameters in the right plot are $i_c = \mathcal{U}(-5°, 5°)$, $\Omega_c = 100°, \omega_c = 10°, i_0 = 45°, e_c = \mathcal{U}(0.1, 0.5)$. Variation of the line of sight shapes the evolution of both observables with largest effects seen when $\omega_c = 270°$. The left peak of the spectral line is more prominent when Ω_c, $\omega_c \leq 180°$ and $e_c > 0.3$, but the right peak dominates when $\omega_c = 270°$. These two orbital parameters significantly influence the amplitude of the differential phase when eccentricity is smaller.

Notable net effects of both orbital shape angles are found when they have larger values simultaneously. These maps can help to extract exceptional features of the BLR structure from future high-resolution observations.

Kovačević et al. (2020b) demonstrated differences between the differential 'zoo' phases of single SMBH and CB-SMBH systems. The differential phases of CB-SMBH appear as two blended and deformed S-shaped signals, asymmetrical along the line center, whose variabilities depend on the orbital motion of clouds and SMBHs. The shape and amplitude of the phases of CB-SMBH systems depend on presumed orbital characteristics of SMBHs and clouds in their BLRs.

An example of a coplanar CB-SMBH system, where clouds of smaller SMBH have anti-aligned angular momenta, and the inclinations of orbits of clouds are linearly spaced between 90° and 175° are given in Fig. 12. It is also clear from the grid of models that if a more substantial number of parameters vary simultaneously, the shapes of differential phases will be more complicated. The randomiza-

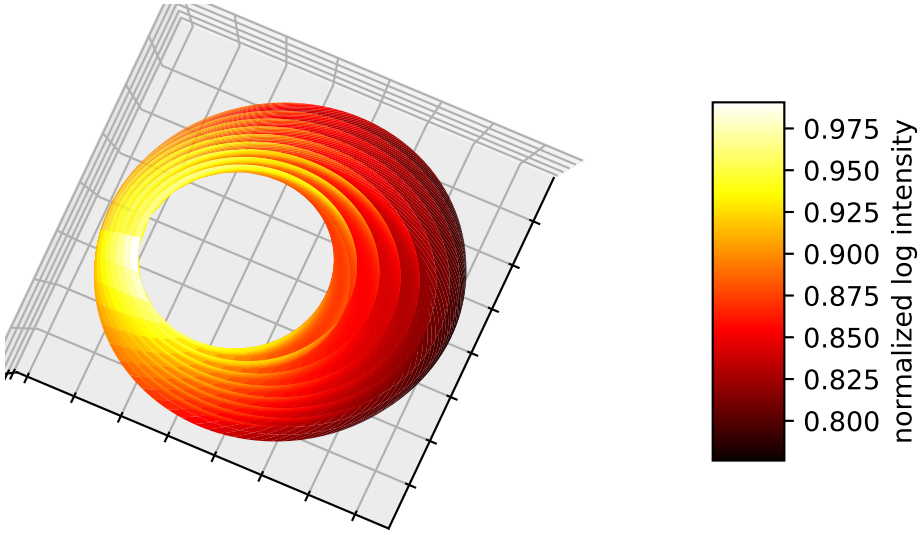

Fig. 8: The normalized intensity distribution for Paα for a single SMBH model. Model parameters are: $M = 6 \times 10^7 M_\odot, i_c = (-10°, 10°), \Omega_c = 180°, \omega_c = 100°$; the inner and outer radii of BLR are given by (20,45) ld.

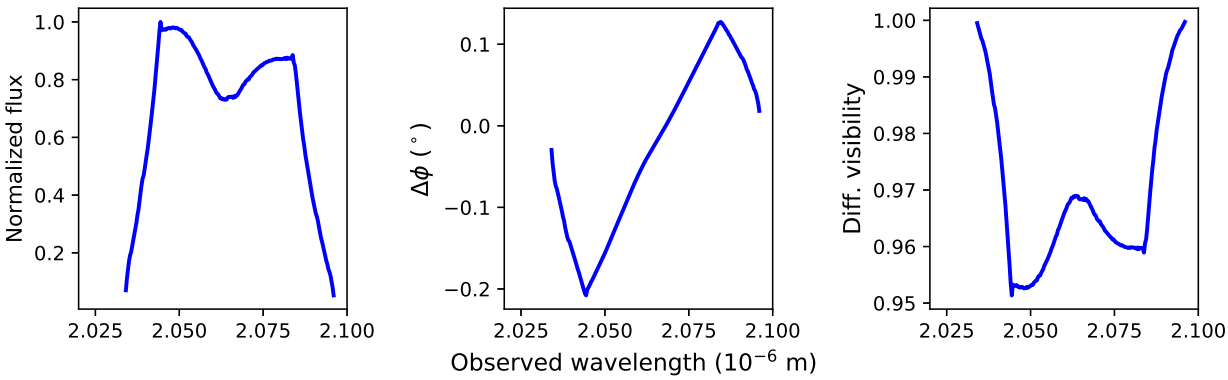

Fig. 9: The effect of elliptical motion of clouds for a single SMBH BLR model given in Fig. 8. Spectrum (*left*), differential phase (*middle*), and differential visibility (*right*) are given for the Paα spectral line.

tion of nodes and apocentres of clouds' orbits in both BLRs affects the forms of both observables. A central whirl is a prominent feature in the right panel. Before proceeding further, we make a digression to an additional consideration. For the line of sight $i_0 = 10°$, the spectral lines have concave wings and narrow core. As i_0 increases, the line shapes broaden with convex sides. Still, differential phases vary drastically in their amplitudes, widths, and forms.

The differential phase signal is sensitive to the position of orbital nodes, inclinations, eccentricities, and arguments of pericentre, along with standardly expected effects related to the geometrical inclination of the observer. The right-skewed distributions of the clouds' orbital eccentricities cause noise effects as small random fluctuations in the differential phase curve. Also, some examples of synthetic spectral lines of a single SMBH are indistinguishable from those obtained from the CB-SMBH system but still have differing differential phases. This implies that the differential phases are markers for CB-SMBH. Observationally for the observer the variability of the differential phase is most substantial for lower inclinations. As much as the central part of the spectral lines is disfigured, the net effect is that the differential phase peaks move away from the line center. The plateau between the differential phase peaks is more prominent. The opposite is valid when there are higher contributions of projected lower velocities in spectral lines. The reversed situation occurs when the line peaks are closer together, when the differential phase peaks move closer to the center of the line. Kovačević et al. (2020b) investigated the effects of anti-aligned clouds' orbital momenta on velocity distributions. Velocity fields are manifested in the closed surface, preserving their topological volume and spatial coherency. For randomly distributed inclinations of the clouds orbit, the velocity fields of such BLRs

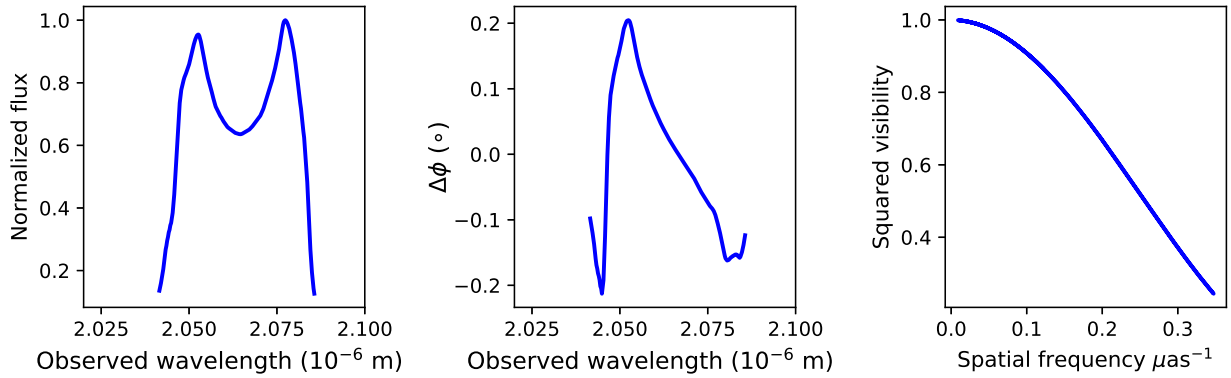

Fig. 10: Interferometric observables for the CB-SMBH model: $M_1 = 6 \times 10^7 M_\odot, M_2 = 4 \times 10^7 M_\odot, i_1 = 5°, i_2 = 0°, e = 0.5, \Omega_{1,2} = 100°, \omega_1 = 190°, \omega_2 = 10°, \omega_{c1} = 100°, \omega_{c2} = 280°, e_c = 0.5, i_c = (-10°, 10°)$. The inner and outer radii of BLRS of larger and smaller SMBHs are (20, 40) ld and (16, 32) ld. Spectrum (*left*), differential phase (*middle*), and squared visibility (*right*) for Paα.

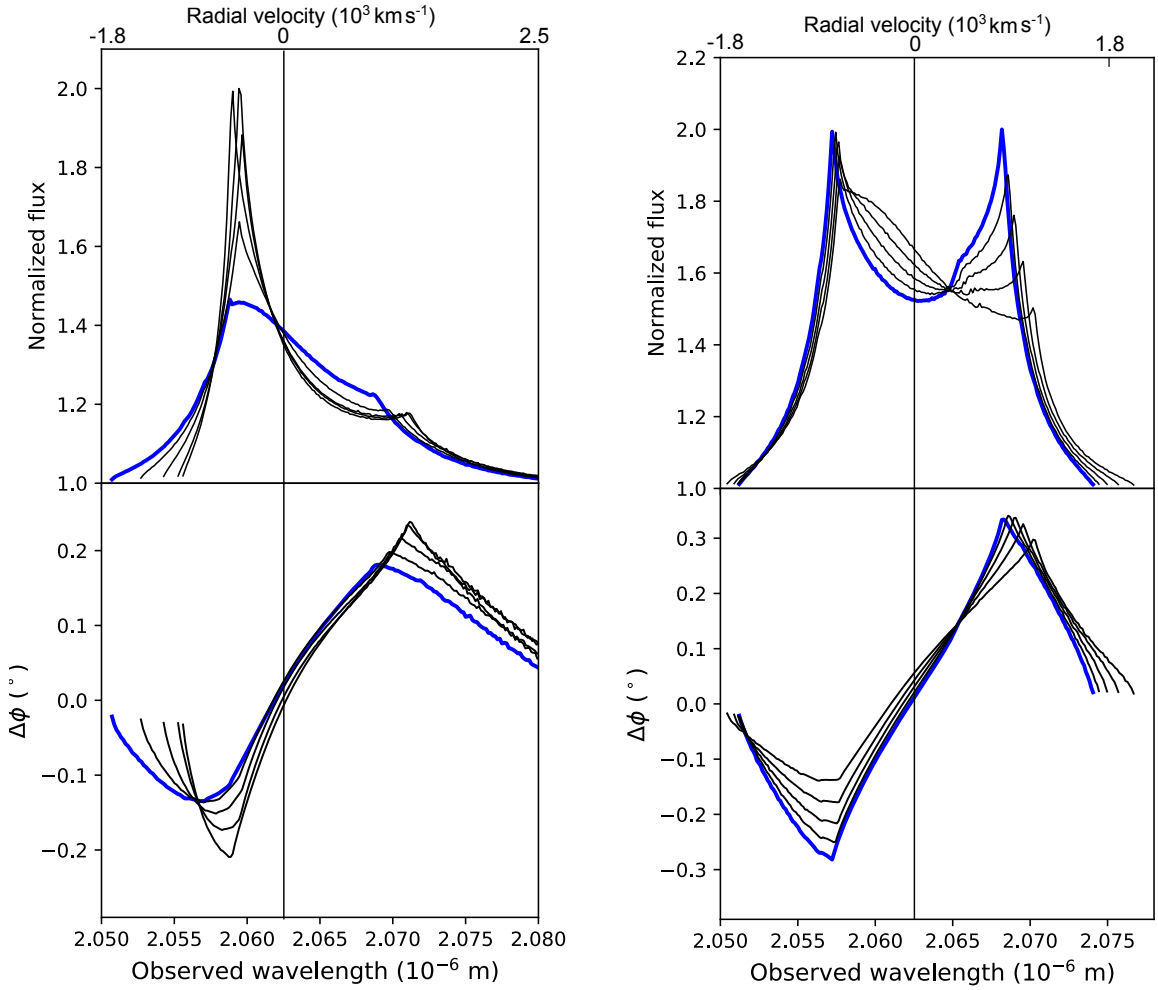

Fig. 11: Evolution of the Paα emission line (upper subplots) and the corresponding differential phase ($\Delta\phi$, lower subplots) as a function of wavelength and radial velocity. Figure adopted from Kovačević et al. (2020b).

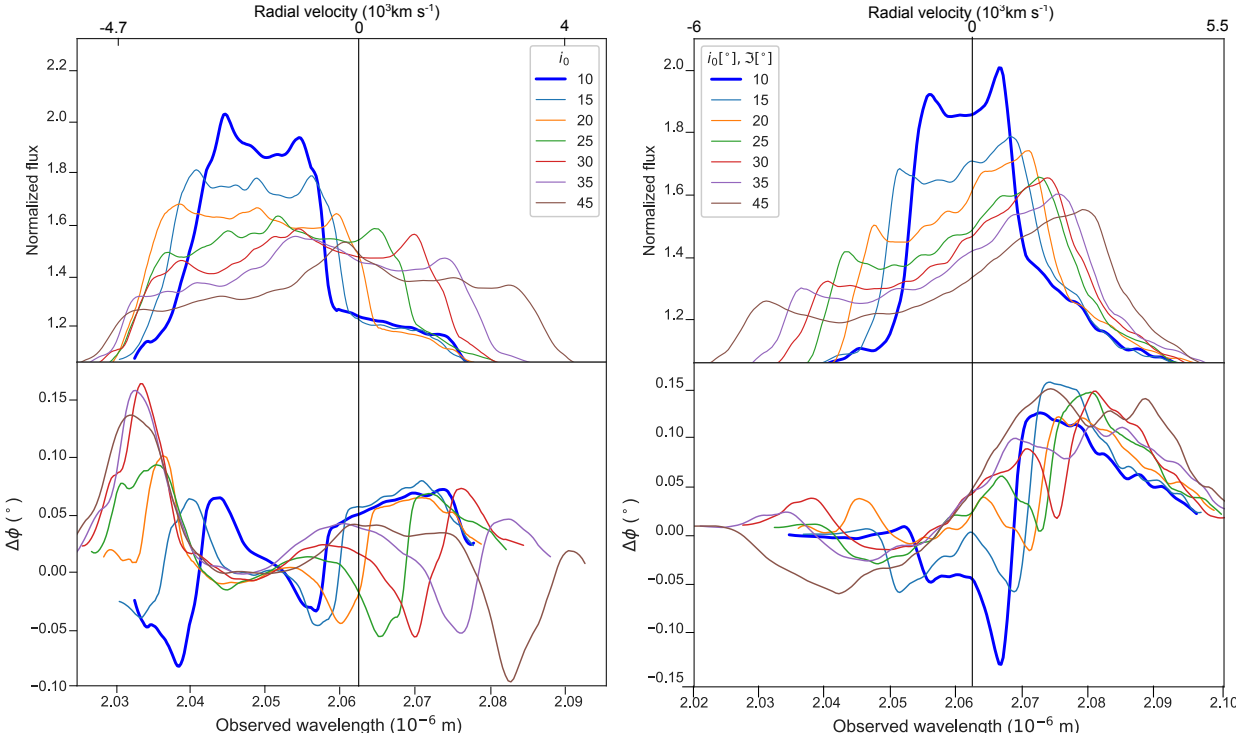

Fig. 12: Evolution of the Paα emission line (upper subplots) and the corresponding differential phase ($\Delta\phi$, lower subplots) as a function of wavelength (or radial velocity) for different models with anti-aligned angular momenta of clouds in the BLR of less massive SMBH in the CB-SMBH system. $\mathcal{C}$ stands for the coplanar CB-SMBH system. $\Im = \mathcal{U}(l, r)$ stands for inclination ranges from $\mathcal{U}(-l, l)$ up to $\mathcal{U}(-r, r)$. The model parameters are: *Left:* $\mathcal{C}, \Omega_k = 100°, \omega_1 = 250°, \omega_2 = 70°, e_k = 0.5, k = 1, 2$; $i_{c1} = \mathcal{U}(-5°, 5°), i_{c2} = \mathcal{U}(90°, 175°), \Omega_c = \mathrm{rnd}(0.1°, 359°)$, $\omega_{c1} = 120°, \omega_{c2} = 300°, e_c = 0.5$; *Right:* $\mathcal{C}, \Omega_k = 100°, \omega_1 = 250°, \omega_2 = 70°, e_k = 0.5, k = 1, 2$; $\Im = \mathcal{U}(10°, 45°), \delta\Im = 5° i_{c2} = \mathcal{U}(90° - 175°), \Omega_c = \omega_c = \mathrm{rnd}(0.1°, 359°)$, $e_c = 0.5$. Adopted from Kovačević et al. (2020b).

are not volume-preserving in the topological sense. For the synchronous alignment of angular momenta of the BLR clouds, the absolute value of clouds' velocities increases toward the outer side lobes of disc-like BLRs. For anti-aligned BLRs, the absolute values for the velocity increase toward sections close to the apocentre and pericentre.

5. OBSERVATIONAL PROSPECTS FOR CB-SMBH

Elvis and Karovska (2002) were the first who proposed a method to determine the direct geometrical distances to radio-quiet quasars that can measure the cosmological constant Λ. In this case, the parallax triangle is inverted with the known length being the dimension of BLR of the distant quasar. Up to now, the GRAVITY observations through spectroastrometry sensitively detect the angular structure of the BLR in the direction perpendicular to the line-of-sight (LOS), whereas the RM observations are more sensitive along the direction of sight. The time lag of an emission line response to the continuum variation is also the radial position of the line emitter with respect to the continuum source. However, two more coordinates are needed to determine the 3D image of the region. Interferometry could provide transverse measurements (Woillez et al. 2003) and two missing coordinates (see Fig. 13). A joint analysis of data collected by both techniques can thus directly measure the AGN absolute angular distances and central black hole masses (Wang et al. 2020). As the Paα and Hβ lines are both from $n = 4$ energy level to $n = 3, 2$, respectively, the Paα regions overlap regions with the Hβ line measured by RM. Moreover, the lengths of GRAVITY observations and RM campaigns are quite different, measuring the variable part and entire regions, respectively. Wang et al. (2020) found that the spectra of 3C 273 are similar in widths and shapes, implying that the GRAVITY-measured regions are about identical to the RM-measured ones. There are projects dedicated to searching for the CB-SMBH electromagnetic signatures. There are just a few monitorings, primarily because of critical technological and practical observational criteria for disentangling the CB-SMBHs signatures. The process of synergy between the RM and interferometry investigations of AGN has already begun. The long-term RM project called

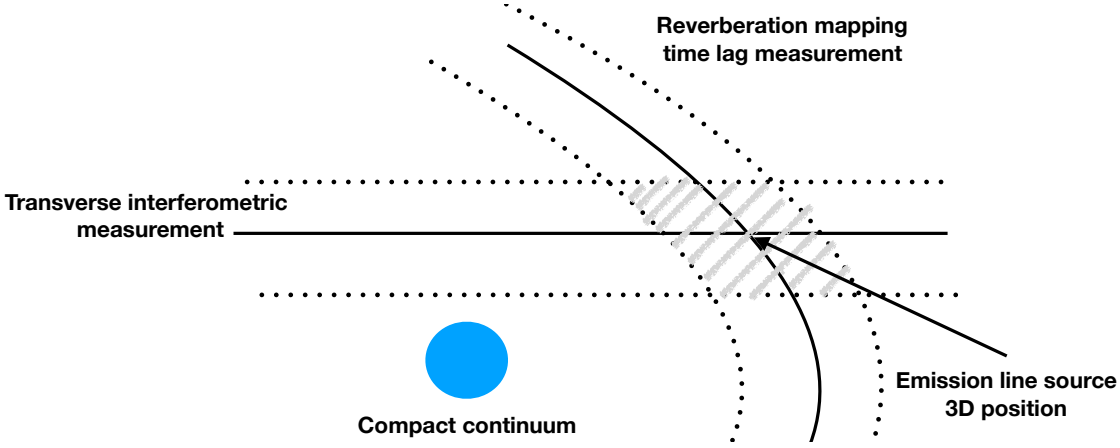

Fig. 13: Broad line region tomography through RM and interferometry. The solid curve represents the RM measurement. The horizontal lines correspond to the interferometry measurement. The blue circle represents a continuum source. The combination of both techniques produces the 3D position of the line-emitting region (shaded polygon).

Monitoring AGNs with Hβ Asymmetry (MAHA) uses the Wyoming Infrared Observatory 2.3 m telescope to explore the geometry and kinematics of the gas responsible for complex Hβ emission-line profiles, which also provides opportunity to search for evidence of CB-SMBH (see Du et al. 2018a, Brotherton et al. 2020). Several candidates (such as Mrk 6 and Ark 120) show potential features for CB-SMBHs. This RM also closely cooperates with the ongoing GRAVITY AGN operations. Eracleous et al. (2012) compiled a list of 88 CB-SMBHs candidates showing significant offsets of the Hβ emission line by thousands of km s^{-1}. Since then, this set of candidates was continuously spectroscopically monitored (see Runnoe et al. 2015, 2017). The study by (Runnoe et al. 2017) presented a catalog of measured radial velocity variations of the broad Hβ lines, radial velocity curves, and derived minimum limits on the total mass of CB-SMBHs based on the hypothesis that the velocity variations arise from the orbital motion. Similar searches for the CB-SMBH candidates based on the multi-epoch SDSS spectroscopy of the broad Hβ line have been completed by (Shen et al. 2013, Liu et al. 2014, Guo et al. 2019). Preparations for the upcoming photometric and spectroscopic surveys (Vera C. Rubin Observatory Legacy Survey of Space and Time (LSST), Manuakea Spectroscopic Explorer (MSE)) are undergoing. Serbian team for the LSST directable software in-kind contribution designed the metrics to estimate the cadence effects on detecting CB-SMBH by upcoming time-domain surveys (LSST and MSE Kovačević et al. 2021a,b). It is estimated that combining rolling cadence operations with powerful deep learning algorithms can lead to detection of a few dozens of the CB-SMBH candidates in the optical domain.

When writing this article, we expect the James Webb Space Telescope (JWST) to accompany the suite of available instruments relevant to the CB-SMBH investigation on October 31, 2021. Its Near-Infrared Imager and the Slitless Spectrograph (JWST-NIRISS) Aperture Masking Interferometry (AMI) mode will permit accurate imaging (i.e., without any prior assumptions on source geometry) at $\sim$ 65 mas angular resolution at centers of AGNs. This is paramount for studying complex extended accretion flows in the vicinity of SMBHs (Ford et al. 2014). A NIRISS AMI mode applied on the low redshift AGN with double-peaked optical emission lines will find dual AGNs at separations of < 35 pc and contrasts of < 10 mag up to ~ 50 Mpc. Thus, NIRISS's AMI will probe binaries closer to the merger and with lower accretion rate (and lower mass) secondary SMBHs (Ford et al. 2014). Ground-based interferometry relies on modeling the amplitude and closure phase based on a priori model of the source, while JWST AMI is capable of inverse Fourier transforming the fully measured complex visibilities (Ford et al. 2014). Significantly, ground-based instruments' meaningful results depend on the model's accuracy, for which the number of free parameters is lesser than the number of equations. Both ground-based and space-born interferometry will revolutionize the extragalactic astronomy because, at < 1 arcsec resolution, we start to see changing structures in AGN which is a qualitatively new view.

6. CONCLUSION

Our current knowledge about CB-SMBHs is increasing, yet on a rudimentary level. There are enormous open questions about CB-SMBHs, which include (but are not limited to): under what conditions are both or only one of the SMBH active implications of two degrees of freedom of CB-SMBH orbital shape on continuum variation, significant uncertainties in evolution timescales of CB-SMBHs, what are the geometry and kinematics of BLRs in CB-SMBH systems. In the sense of spectral line shapes, the sources share many similarities and may not always appear as different to the single accreting SMBH so-

urces as one would expect. The key differences can be found at resolution < 1 arcsec when changing structures start to appear in interferometric observables, as we showed here. Such modeling is essential for selecting putative signatures that may guide present and future surveys.

We reviewed several possible observational signatures of CB-SMBHs from numerical simulations. Although there are not yet proven CB-SMBHs, searches for CB-SMBHs through various channels of multi-messenger techniques are appealing. We expect that the identifications of CB-SMBHs may have lead to detection of GWs. Some indices point out a probable non-zero eccentricity for some CB-SMBH emitting GWs. A mechanism that could lead to eccentric mergers is the Kozai–Lidov oscillation (Wen 2003), where a distant third object perturbs the binary orbital motion. Theoretically a continuous-GW detection by PTAs could yield a measurement of the system's orbital frequency and eccentricity (Burke-Spolaor et a. 2019) but no other CB-SMBH orbital elements. However, chirp mass and source distance cannot be directly measured unless the orbital frequency evolution is observed throughout the PTA observations or if the host galaxy of the continuous-wave source is identified (Burke-Spolaor et a. 2019). In data collected over 13 years, the North American Nanohertz Observatory for Gravitational Waves (NANOGrav) has found an intriguing low-frequency signal (Arzoumanian et al. 2020). The study examined potential implications for the supermassive black hole binary population under the hypothesis that the signal is indeed astrophysical. In this light, independent electromagnetic observational techniques have to be involved, such as the reverberation mapping technique and spectroastrometry technique with a high spatial resolution (realized at the GRAVITY/VLTI and JWST). Combined with growing and improved theoretical predictions for electromagnetic and GW signatures, there are great promises for detecting CB-SMBHs in the following decades. This will then open up a new chapter in studies of cosmic growth and evolution of SMBHs.

Acknowledgements – The author thanks the Editors and prof. Luka Č. Popović for their insightful suggestions that contributed to a much-improved manuscript. Furthermore, the author wishes to address a special thank to prof. Dragana Ilić for supporting. Author acknowledges the funding provided by the Faculty of Mathematics University of Belgrade (the Ministry of Education, science and technological development of Republic Serbia contract 451-03-9/2021-14/200104). Author also acknowledges the support by The Chinese Academy of Sciences President's International Fellowship Initiative (PIFI) for visiting scientist.

REFERENCES

Antonucci, R. 1993, ARA&A, 31, 473

Arzoumanian, Z., Baker, P. T., Blumer, H., Becsy, B., et al. 2020, ApJ, 905, L34

Begelman, M. C., Blandford, R. D. and Rees, M. J. 1980, Natur, 287, 307

Bentz, M. C. 2016, AGN Reverberation Mapping. In: Boffin H., Hussain G., Berger J. P., Schmidtobreick L. (eds) Astronomy at High Angular Resolution. Astrophysics and Space Science Library, vol 439. (Cham, Switzerland: Springer)

Best, P. N., Kauffmann, G., Heckman,T. M., Brinchmann, J., Charlot, S., Ivezić, Ž. and White, S. D. M. 2005, MNRAS, 362, 25

Blandford, R. and McKee, C. 1982, ApJ, 255, 419

Blandford, R. D., Netzer, H., Woltjer, L., Courvoisier, T. J.-L. and Mayor, M. 1990, Active Galactic Nuclei, (Berlin, Heidelberg: Springer-Verlag)

Bogdanović, T., Reynolds, C. S. and Miller, M. C. 2007, ApJ, 661, L147

Bon, E., Jovanovicć, P., Marziani, P., Shapovalova, A. I., et al. 2012, ApJ, 759, 118

Bon, E., Zucker, S., Netzer, H., Marziani, P., et al. 2016, ApJS, 225, 29

Brotherton, M. S., Du, P., Xiao, M., Bao, D-W., et al. 2020, ApJ, 905, 77

Burke-Spolaor, S., Taylor, S. R., Charisi, M., Dolch, T., et al. 2019, A&ARv, 27, 5

Chandrasekhar, S. 1943, ApJ, 97, 255

Charisi, M., Bartos, I., Haiman, Z., Price-Whelan, A. M., et al. 2016, MNRAS, 463, 2145

Delaa, O. Zorec, J., Domiciano de Souza, D., Mourard, D., Perrau, K., et al. 2013, A&A, 555, A100

De Rosa, A., Vignali, C., Bogdanović, T., Capelo, P. R., Charisi, M., et al. 2019, NewAR, 86, 101525

Du, P., Brotherton, M. S., Wang, K., Huang, Z.-P., Hu, C., Kasper, D. H., Chick, W. T., et al. 2018a, ApJ, 869, id. 142

Du, P., Zhang, Z. X., Wang, K., Huang, Y. K., et al. 2018b, ApJ, 856, 6

Elvis, M. and Karovska, M. 2002, ApJ, 581, L67

Eracleous, M., Livio, M., Halpern, J. P. and Storchi-Bergmann, T. 1995, ApJ, 438, 610

Eracleous, M., Boroson, T. A., Halpern, J. P. and Liu, J. 2012, ApJS, 201, 23

Feng, H. C., Hu, C., Li, S.-S., Liu, H. T., et al. 2021, ApJ, 909, id. 18

Ford, K. E. S., McKernan, B., Sivaramakrishnan, A., Martel, A. R., et al. 2014, ApJ, 783, 73

Graham, M. J., Djorgovski, S. G., Stern, D., et al. 2015, MNRAS, 453, 1562

GRAVITY Collaboration Sturm, E., et al. 2018, Natur, 563, 657

GRAVITY+ Collaboration Eisenhauer, F., Garcia, P., Genzel, R., Hönig, S., et al. 2019, GRAVITY+: Towards Faint Science, All Sky, High Contrast, Milli-Arcsecond Optical Interferometric Imaging, White Paper and Proposal

GRAVITY Collaboration Pfuhl, O., et al. 2020a, A&A, 634, A1

GRAVITY Collaboration Dexter, J., et al. 2020b, A&A, 635, A92

GRAVITY Collaboration Amorim, A., et al. 2020c, A&A, 643, A154
Grier, C. J., Trump, J. R., Shen, Y., Horne, K., et al. 2017, ApJ, 851, 21
Guo, H., Liu, X., Shen, Y., et al. 2019, MNRAS, 482, 3288
Haiman, Z., Kocsis, B. and Menou, K. 2009, ApJ, 700, 1952
Hönig, S. F., Alonso Herrero, A., Gandhi, P., Kishimoto, M., et al. 2018, ExA, 46, 413
Ilić, D., Shapovalova, A. I., Popović, L. Č., Chavushyan, V., et al. 2017, FrASS, 4, 12
Ilić, D., Oknyansky, V., Popović, L. Č., Tsygankov, S. S., et al. 2020, A&A, 638, id. A13
Jaffe, W., Meisenheimer, K., Rottgering, H. J. A., Leinert, C. H., et al. 2004, Natur, 429, 47
Just, A., Khan, F. M., Berczik, P., Ernst, A. and Spurzem, R. 2011, MNRAS, 411, 653
Kaspi, S., Brandt, W. N., Maoz, D., Netzer, H., Schneider, D. P. and Shemmer, O. 2007, ApJ, 659, 997
Kishimoto, M. Hönig, S., Antonucci, R., Barvainis, R., et al. 2011 A&A, 527, 121
Kollmeier, J., Anderson, S. F., Blanc, G. A., Blanton, M. R., et al. 2019, BAAS, 51, id. 274
Kovačević, A., Popović, L. Č., Shapovalova, A. I. and Ilić, D. 2017, Ap&SS, 362, id. 31
Kovačević, A. B., Pérez-Hernández, E., Popović, L. Č., Shapovalova, A. I., Kollatschny, W. and Ilić, D. 2018, MNRAS, 475, 2051
Kovačević, A. B., Popović, L. Č., Simić, S. and Ilić, D. 2019, ApJ, 871, id. 32
Kovačević, A. B., Wang, J.-M. and Popović, L. Č. 2020a, A&A, 635, id. A1
Kovačević, A. B., Songsheng, Y.-Y., Wang, J.-M. and Popović, L. Č. 2020b, A&A, 644, A88
Kovačević, A. B., Yi, T., Dai, X., Yang, X., Čvorović-Hajdinjak, I. and Popović, L. Č. 2020c, MNRAS, 494, 4069
Kovačević, A. B., Popović, L. Č. and Ilić, D. 2020d, OAst, 29, 51
Kovačević, A., Ilić, D., Popović, L. Č., Jankov, I., et al. 2021a, accepted for publication in MNRAS
Kovačević, A., Ilić, D., Jankov, I., Popović, L. Č., et al. 2021b, submitted to LSST SCOC
Li, Y.-R., Wang, J.-M., Ho, L. C., Lu, K.-X., et al. 2016, ApJ, 822, 4
Li, Y.-R., Wang, J.-M., Zhang, Z.-X., Wang, K., et al. 2019, ApJS, 241, 33
Liu, T., Gezari, S., Ayers, M., et al. 2019, ApJ, 884, 36
Liu, X., Shen, Y., Bian, F., Loeb, A. and Tremaine, S. 2014, ApJ, 789, 140
Mangham, S. W., Knigge, C., Williams, P., et al. 2019, MNRAS, 488, 2780
Marconi, A., Maiolino, R. and Petrov, R. G. 2003, Ap&SS, 286, 245
Marconi, A., Risaliti, G., Gilli, R., Hunt, L. K., Maiolino, R. and Salvati, M. 2004, MNRAS, 351, 169
Martini, P. 2004, Coevolution of Black Holes and Galaxies, from the Carnegie Observatories Centennial Symposia, Ed. by L. C. Ho. (Cambridge: Cambridge University Press.), 169
Netzer, H. 2013, The Physics and Evolution of Active Galactic Nuclei (Cambridge: Cambridge University Press)
Netzer, H. 2015, ARA&A, 53, 365
Padovani, P., Alexander, D. M., Assef, R. J., De Marco, B., Giommi, P., Hickox, R. C., et al. 2017, A&ARv, 25, 2
Peterson, B. M. 1998, AdSpR, 21, 57
Peterson, B. M. 2014, SSRv, 183, 253
Peterson, B. M., Ferrarese, L., Gilbert, K. M., Kaspi, S., et al. 2004, ApJ, 613, 682
Petrov, R. G., Malbet, F., Richichi, A., et al. 2001, CRPhy, 2, 67
Petrov, R. G., Millour, F., Lagarde, S., Vannier, M., Rakshit, S., Marconi, A. and Weigelt, G. 2012, in Proc. SPIE 8445, Optical and Infrared Interferometry III, ed. F. Delplancke, J. K. Rajagopal, and F. Malbet 84450W-1
Popović, L. Č. 2012, NewAR, 56, 74
Popović, L. Č. 2020, OAst, 29, 1
Popović, L. Č., Mediavilla, E. G. and Pavlović, R. 2000, SerAJ, 162, 1
Popović, L. Č., Shapovalova, A. I., Ilić, D., Kovačević, A., Kollatschny, W., et al. 2011, A&A, 528, id. A130
Popović, L. Č., Shapovalova, A. I., Ilić, D., Burenkov, A., et al. 2014, A&A, 572, id. A66
Rakshit, S., Petrov, R. G., Meilland, A. and Hönig, S. F. 2015, MNRAS, 447, 2420
Rees, M. J. 1984, ARA&A, 22, 471
Runnoe, J. C., Eracleous, M., Mathes, G., Pennell, A., et al. 2015, ApJS, 221, id. 7
Runnoe, J. C., Eracleous, M., Pennell, A., et al. 2017, MNRAS, 468, 1683
Salpeter, E. E. 1964, ApJ, 140, 796
Shapovalova, A. I., Popović, L. Č., Collin, S., Burenkov, A. N., et al. 2008, A&A, 486, 99
Shapovalova, A. I., Popović, L. Č., Chavushyan, V. H., Burenkov, A. N., Ilić, D., et al. 2016, ApJS, 222, id. 25
Shapovalova, A. I., Popović, L. Č., Afanasiev, V. L., Ilić, D., Kovačević, A., et al. 2019, MNRAS, 485, 4790
Shen Y. and Loeb, A. 2010, ApJ, 725, 249
Shen, Y., Liu, X., Loeb, A. and Tremaine, S., 2013, ApJ, 775, 49
Songsheng, Y.-Y., Wang, J.-M., Li, Y.-R. and Du, P. 2019, ApJ, 881, 140
Swain, M., Vasisht, G., Akeson, R., Monnier, J., et al. 2003, ApJ, 596, L163
Swann, E., Sullivan, M., Carrick, J., et al. 2019, Msngr, 175, 58
Urry, C. M. and Padovani, P. 1995, PASP, 107, 803
Volonteri, M., Haardt, F. and Madau, P. 2003, ApJ, 582, 559
Waisberg, I., Dexter, J., Pfuhl, O., Abuter, R., Amorim, A., Anugu, N., et al. 2017, ApJ, 844, 72
Wang, F., Yang, J., Fan, X., Hennawi, J. F., et al 2021, ApJ, 907, L1
Wang, J.-M. and Bon, E. 2020, A&A, 643, L9

Wang, J.-M. and Li, Y.-R. 2020, RAA, 20, 160
Wang, J.-M., Chen, Y.-M., Hu, C., et al. 2009, ApJ, 705, L76
Wang, J.-M., Songsheng, Y.-Y., Li, Y.-R. and Yu, Z. 2018, ApJ, 862, 171
Wang, J.-M., Songsheng, Y.-Y., Li, Y.-R., Du, P. and Zhang, Z.-X. 2020, NatAs, 4, 517
Wang, J. and Ip, W.-H. 2020, RAA, 20, 157
Wang, M.-X., Luo, A.-L., Song, Y.-H., et al. 2019, MNRAS, 482, 1889
Weigelt, G., Hofmann, K. -H., Kishimoto, M., Hönig, S., et al. 2012, A&A, 541, L9
Wen, L. 2003, ApJ, 598, 419
Wittkowski, M., Kervella, P., Arsenault, R., Paresce, F., et al. 2004, A&A, 418, L39
Woillez, J., Sol, H., Lai, O., Guyon, O. and Perrin, G. 2003, in Proceedings of SPIE - The International Society for Optical Engineering, 4838(2), 1389
Zeldovich, Ya. B. and Novikov, I. D. 1964, Dokl. Akad. Nauk SSSR, 155, 1033

ИЗУЧАВАЊЕ ТЕСНО ДВОЈНИХ СУПЕРМАСИВНИХ ЦРНИХ РУПА У ВИСОКОЈ УГЛОВНОЈ РЕЗОЛУЦИЈИ

A. Kovačević[1,2]

[1] *Department of Astronomy, Faculty of Mathematics, University of Belgrade Studentski trg 16, 11000 Belgrade, Serbia*

[2] *Fellow of Chinese Academy of Sciences President's International Fellowship Initiative (PIFI) for visiting scientist*

E–mail: *andjelka@math.rs*

УДК 524.882 : 524.7
Прегледни рад по позиву

Очекује се да ће гравитациони таласи (ГТ) у домену нанохерца (nHz) потицати од тесно двојних супермасивних црних рупа (ТД-СМЦР где су компоненте са кеплеровским кретањем на међусобној удаљености мањој од $\sim$ 0.1 pc), а које су реликти судара галаксија, и уз то се предпоставља да ће се детектовати техником познатом као пулсарски временски низ (ПВН, енг. Pulsar Timing Array (PTA)). Изазов у досадашњим потрагама за ТД-СМЦР је у томе што њихове отиске (сигнатуре) у подацима није лако одвојити од индивидуалних СМЦР. ПВН ће имати увид у ране фазе бинарне еволуције само за фреквенције потекле од бинарног система са довољно великом масом и великом почетном ексцентричношћу. Стога морамо користити и посматрања у електромагнетном подручју, како бисмо одредили орбиталне параметре ових система и тестирали својства nHz ГТ. 2Д реверберационо мапирање (РМ) је моћан алат за испитивање кинематичких својстава и геометријских карактеристика расподеле јонизованог гаса у близини СМЦР (појединачне или двојне), али која може ипак изгубити део информација због пројекције на линију визуре посматрача. Међутим, спектроастрометрија доступна на инструментима AMBER и GRAVITY и њиховим долазећим наследницима омогућиће независно мерење димензија, геометрије и кинематике емисионог региона СМЦР. Комбиновањем ове две технике биће могуће разрешити детекцију ТД-СМЦР. У овом прегледу ћемо размотрити РМ и спектроастрометријске посматрачке отиске (сигнатуре) ТД-СМЦР које имају значајну ексцентричност, а које су добијене из скорашњих симулација, поклањајући при том посебну пажњу отвореним питањима.